Journal of Power Sources 189 (2009) 101–107

Contents lists available at ScienceDirect

Journal of Power Sources

journal homepage: www.elsevier.com/locate/jpowsour

Effects of entropy changes in anodes and cathodes on the thermal behavior of lithium ion batteries

Ralph E. Williford, Vilayanur V. Viswanathan, Ji-Guang Zhang*

Pacific Northwest National Laboratory, P.O. Box 999, Richland, WA 99352, USA

ARTICLE INFO

Article history:
Received 29 July 2008
Received in revised form 11 October 2008
Accepted 13 October 2008
Available online 5 November 2008

Keywords:
Lithium ion battery
Thermal property
Entropy
Electric vehicles
High power
Safety

ABSTRACT

The entropy changes (ΔS) in various cathode and anode materials, as well as complete Li-ion batteries, were measured using an electrochemical thermodynamic measurement system (ETMS). A thermal model based on the fundamental properties of individual electrodes was used to obtain transient and equilibrium temperature distributions of Li-ion batteries. The results from theoretical simulations were compared with results obtained in experimental measurements. We found that the detailed shape of the entropy curves strongly depends on the manufacturer of the materials even for the same nominal compositions. $LiCoO_2$ has a much larger entropy change than $LiNi_xCo_yMn_zO_2$. This means that $LiNi_xCo_yMn_zO_2$ is much more thermodynamically stable than $LiCoO_2$). The temperatures around the positive terminal of a prismatic battery are consistently higher than those at the negative terminal, due to differences in the thermal conductivities of the different terminal connectors. When all other simulation parameters are the same, simulations that use a battery-averaged entropy tend to overestimate the predicted temperatures when compared with simulations that use individual entropies for the anode and the cathode, due to computational averaging.

1. Introduction

High-power secondary batteries for plug-in hybrid electric vehicle applications generate much more heat during rapid charge and discharge cycles at high current levels, such as during quick acceleration when the battery consumes power or during deceleration or quick stops when the battery is charged using recovered inertial energy [1]. However, most previously used lithium batteries operated at low discharge rates. The use of these batteries at high power rates will pose serious thermal-stability problems, especially when the battery size increases and many batteries are interconnected to form large packages. Toyota recently announced that because of these safety concerns, it will delay by 1–2 years the launch of new high-mileage hybrid vehicles equipped with Li-ion battery technology [2]. As battery size increases, the ratio of cooling area to heat generating volume decreases, and as charge/discharge current increases, more heat is generated. The temperature of the battery thus rises dramatically, leading to the possibility that internal temperatures will exceed permissible levels. The transient variation of the temperature distribution in the battery during operation should therefore be considered during development of large Li-ion secondary batteries.

In a model established two decades ago, Bernardi et al. [3] described a general energy balance equation for battery systems. This rather complete system of equations laid the foundations for the prediction of cell temperatures and heat generation resulting from electrochemical reactions, phase changes, mixing effects, and Joule heating. In 1993, Doyle et al. [4] developed a microscale continuum model of the galvanostatic charge and discharge of Li/polymer/porous cathode cells using concentrated solution theory. In that model, they simulated insertion of Li into the cathode using superposition of concentration fields to simplify the calculations. Concentration and charge distributions across the anode/electrolyte/cathode assembly were predicted, but thermal performance was not. Their work was followed by a series of papers focused on thermal performance. Assuming uniform heat generation throughout the battery, superposition methods were again employed by Newman and Tiedemann [5] to compute the temperature rise for a range of aspect ratios in a three-dimensional battery. Methods for treating time-dependent heat generation rates were also discussed, but material temperature dependencies were not treated. In a later report, Pals and Newman [6] established a one-dimensional model for a single cell and for stack thermal performance. Material properties were temperature dependent. The entropic term in the heat generation rate was recognized, but deleted from the analysis because insufficient data were available

* Corresponding author at: Pacific Northwest National Laboratory, Energy & Environment Directorate, P.O. Box 999, Richland, WA 99352, USA. Tel.: +1 509 372 6515; fax: +1 509 375 3864.
E-mail address: jiguang.zhang@pnl.gov (J.-G. Zhang).

0378-7753/$ – see front matter © 2008 Elsevier B.V. All rights reserved.
doi:10.1016/j.jpowsour.2008.10.078

for the computations. Consequently, the heat generation rate was essentially constant for each simulation. Spatial distributions of temperature and ion concentrations were produced for the stack model. In 1996, Doyle et al. [7] returned to more detailed simulations of local electrochemistry and ion concentration distributions. Others addressed the thermal performance of lithium ion batteries. Funahashi et al. [8] solved for transient temperatures using bulk properties, and uniform heat generation over the battery, but only C_p was temperature dependent. Thomas and Newman [9] found the effects of the heat of mixing to be negligible in a well-designed battery, using a very complete, one-dimensional analysis. Araki et al. [10] used a one-dimensional model with lumped parameters for NiMH battery thermal predictions. Onda et al. [11] modelled a one-dimensional (radial) battery transient with lumped parameters. Inui et al. [12] developed transient two-dimensional and three-dimensional models for temperature, charge state, and current as a function of position. Although their method appears to have been a numerical solution of simultaneous equations, they do not describe the mathematical technique they used.

Theoretical predictions of important physical properties have also recently become available. Kim and Pyun [13] used a Monte Carlo approach to determine basic thermodynamic quantities (internal energy, entropy) for Li intercalation in $Li_{1-x}Mn_2O_4$ electrodes, obtaining good agreement with experimental results. Thermodynamic properties also are available for Li_xCoO_2 [14] and for Li intercalation into carbons [15]. Extensions to three-dimensional thermal performance of batteries have been extensively addressed by Pesaran et al. [16,17] at the National Renewal Energy Laboratory. They successfully simulated thermal behavior of a cylindrical Li-ion battery assuming that the core material (cathode/separator/anode) consisted of a homogenous material with average properties for resistivity, thermal conductivity, and entropy. They also investigated various ventilation methods for battery cooling. They used the finite element method to model the complete battery system, including external heat transfer. In these studies, entropy changes in battery electrodes were recognized as an important factor that may significantly affect the thermal behavior of Li-ion batteries. For example, Hong et al. [18] indicated that the entropy change may contribute more than 50% of the total heat at the C/1 discharge rate. However, the entropy changes in previous studies have been assumed to be uniform parameters for complete batteries, partly because entropy data for individual electrodes were not available. Recently, Yazami [19] developed an approach for the measurement of entropy and enthalpy changes in electrode materials (such as $LiCoO_2$, $LiFePO_4$, and graphite).

To predict more detailed thermal behavior for a battery with different cathode and anode materials, it is necessary to develop a versatile model based on the individual properties (including entropy changes) of the cathode and anode separately. This model can be used not only to simulate the thermal properties of existing batteries, but also to predict the internal temperature of the battery as a function of battery chemistry, state of charge (SOC), power, and battery geometries. Such an improved model will help developers in industry design a new-generation battery that minimizes heat generation and thermal fluctuations, therefore significantly reducing heat-induced failures.

2. Simulation of the thermodynamic behavior of lithium ion batteries

2.1. Model description

The thermodynamic properties (entropy change, ΔS) of cathodes and anodes materials published recently by Yazami [19] were used in an initial effort to simulate the thermal behavior of batteries. The transient temperature distribution of the battery can be solved from the following differential equation:

$$\rho(x)C_p(x,T(x,t))\frac{\partial T(x,t)}{\partial t} = -\nabla[-k(x,T(x,t))\nabla T(x,t)]+\dot{Q}(x,T(x,t)) \quad (1)$$

where

$$\dot{Q}(x,T(x,t)) = R(x,T(x,t))I(x,t)^2 - T(x,t)\Delta S(x,T(x,t))\frac{I(x,t)}{nF} \quad (2)$$

is the space- and temperature-dependent heat generation rate. The model variables are time dependent through their dependence on the temperature and current, which are time dependent. It should be noted that the effects of the heat of mixing, heat effects due to possible chemical reactions, and convective effects are neglected in the model. The first term in Eq. (2) is the rate of heat generated from ohmic heating. The second term is the rate of heat generated from micro-structural (entropic) changes. The rate of heat generated in the electrode or battery can be obtained by integrating Eq. (2) over the electrode or battery volume. To simplify the comparison with experimental results (which normally plots temperature of the battery as a function of the SOC), in the simulations we used depth of discharge (DOD) (DOD = 1 − SOC) as the independent variable to replace time t in Eq. (1). We took this approach because DOD varies linearly with time (t) under constant the current conditions used in our experiment (DOD = $-Jt/C$), where C is the battery capacity (As) and J is the constant current (A). The differential equation employed in the simulations was

$$-\frac{J}{C}\frac{\partial T}{\partial DOD} = \frac{1}{r^\beta}\frac{\partial}{\partial r}\left[\alpha_i r^\beta \frac{\partial T}{\partial r}\right] + \frac{\partial}{\partial z}\left[\alpha_i \frac{\partial T}{\partial z}\right] + \dot{Q}(T,DOD)\frac{\alpha_i}{k_i} \quad (3)$$

where i denotes the material (package, anode, cathode, etc.); $\alpha = k/\rho C_p$ is the thermal diffusivity for each material; $\beta = 0$ or 1 for rectangular or cylindrical coordinates, respectively; z is the axial coordinate; r is the thickness coordinate; T is temperature; and $\dot{Q}$ is the heat generation rate for each material:

$$\dot{Q}_i = I^2 R_i - T\,\Delta S\frac{I}{nF} \quad (4)$$

where I is the current density (A cm^{-2}), R_i is the material resistivity (Ω-cm), T is temperature (K), ΔS is entropy change (J mole^{-1} K^{-1}), n equals one electron per reaction, and F is the Faraday constant (96,485 C mole^{-1}). Finite difference methods for solving Eq. (3) have been investigated by Melgaard and Sincovec [20], including the body, edges, and corners of the battery. It is perhaps noteworthy that the heat-transfer equation they treated accounts for spatial variations in the thermal diffusivities, α. The above equations can be applied to the cathode, separator, and anode, respectively, and matched by boundary conditions. In a typical $LiCoO_2$/C battery, the overall electrochemical reaction can be expressed as

$$2Li_{0.5}CoO_2 + LiC_6 \leftrightarrow 2Li_{0.5+x}CoO_2 + Li_{1-2x}C_6 \quad (5)$$

The corresponding entropy change in this battery can be expressed as

$$\Delta S_{cell} = \Delta S_{Li_{0.5+x}CoO_2} + \Delta S_{Li_{1-2x}C_6} \quad (6)$$

The total heat generated from the $LiCoO_2$ cathode and the carbon anode from their micro-structural changes can be calculated from Eqs. (4) and (6). Fig. 1 shows the entropy changes in a typical $LiCoO_2$/C battery in various charge states (entropy data are taken from Refs. [14] and [19], respectively). The term x on the x-axis of Fig. 1 represents the electrode-averaged ion concentration in $LiCoO_2$ and carbon electrodes. It is important to notice that the spikes in the entropy changes, which correspond to the spikes in

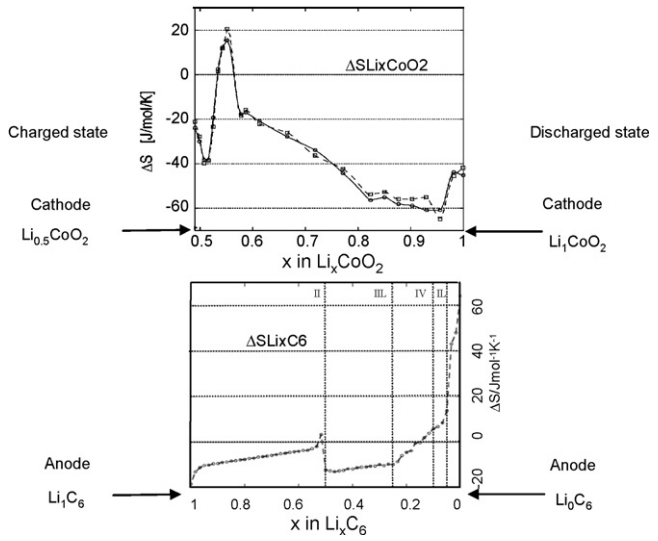

Fig. 1. Entropy changes in a typical $LiCoO_2$/C battery in various charge states. Entropy data for (a) $LiCoO_2$ and (b) graphite are taken from Refs. [13] and [18], respectively.

heat generation, in the cathode and anode strongly depend on the structural properties of the materials [9]. Apparently, if both thermal spikes in the cathode and anode in a battery appear at the same time, the battery will experience large thermal stresses that can lead to early failure or explosions. However, appropriate selection of anode/cathode pairs and their molar ratios can effectively avoid the simultaneous appearance of anode and cathode spikes in a battery, therefore eliminating an important source of overheating during battery operation. The objective of this paper is to enable the 'virtual simulation' of such selections by computer simulations, thus avoiding the expense of actually building many new battery prototypes during material development efforts.

2.2. Boundary conditions

In Cartesian coordinates ($\beta = 0$), the boundary conditions can be expressed generally as

$$aT + b\frac{\partial T}{\partial x} = c \tag{7}$$

where x equals r or z in the thickness direction, and a, b, and c are at least piecewise continuous functions of the spatial dimensions. Fig. 2 shows schematic of boundary conditions for an x–z section

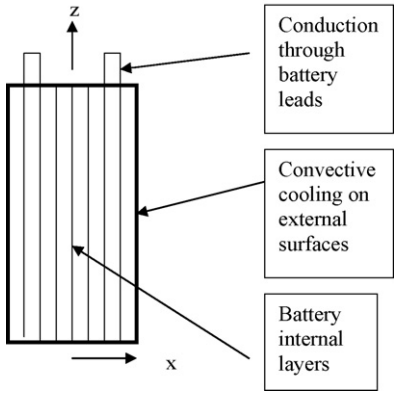

Fig. 2. Schematic of boundary conditions for an x–z section through a prismatic battery. The large flat face of the battery is normal to the plane of the page.

through a prismatic battery (not to scale). The large flat face of the battery is normal to the plane of the page. Eq. (7) is a general form that encompasses all three types of boundary conditions. Examples of straightforward applications are: when $a = 0$ the boundary conditions are von Neumann type; when $b = 0$, the boundary conditions are Dirichlet type; and when a and b are both nonzero, Cauchy conditions prevail. For a full two-dimensional model of the axial and thickness directions for a prismatic battery, including the electrical leads, the following boundary conditions are used. Natural convective cooling by air is assumed to dominate cooling on the exterior surface of the battery. For a convective heat-transfer coefficient, h_{cool}, and an ambient air temperature, T_{air}, the boundary parameters are $a = -h_{cool}$, $b = -k_{ri}$, $c = -h_{cool}T_{air}$ at the right hand battery face, where k_{ri} is the thermal conductivity of the package in the radial (thickness) direction. At the left face, the sign of b is reversed for mathematical self-consistency of the temperature gradients. The convective heat-transfer coefficient for laminar flow of air along a vertical surface is [21]:

$$h_{cool} = C\left(\frac{\Delta T}{L}\right)^n \tag{8}$$

where C and n are constants, L is the height of the battery, and the temperature difference is again from the surface to the ambient air. The effects of the battery electrical leads are also included on the upper edge of the battery, by conductive heat-transfer pathways located just inside the battery package layers. The pathway for the anode is copper, while the pathway for the cathode is aluminum. In this case, $a = -k_M/\Delta x$, $b = -k_{ze}$, and $c = -k_M\, T_{wire}/\Delta x$, where k_M is the axial conductivity of the appropriate lead wire, and T_{wire} is the measured temperature of the lead wire at a distance of Δx from the battery edge.

2.3. Material properties

The material properties (e.g., thermal conductivities, electrical resistivities, etc.) differ greatly between the various materials, which can lead to numerically 'stiff' problems and slow computations. As in most numerical simulations of multi-layered lithium batteries, the properties are 'lumped' into electrode units with effective properties that exhibit less variation. In the present case, the repeating electrode units consisted of separator/electrode/metal/electrode assemblies. The effective properties, such as thermal diffusivities, were calculated by volume averages for both the thickness (i.e., the direction of the current flow) and the axial directions. Additional details are given below. Effective electrical resistivities in the radial (conduction) direction were calculated for electrode assemblies (i.e., separator/electrode/metal/electrode), assuming that the porous separator was dominated by the electrolyte resistivity, using the following equation:

$$r_{assembly}^{radial} = \frac{\sum r_i t_i}{\sum t_i} \tag{9}$$

where t_i is the thickness of the layer in the assembly, r_i is the electrical resistivity of the solid material for the electrode and metal, and

$$r_i = \frac{r_{electrolyte}}{p} + \frac{r_{solid}}{1-p} \tag{10}$$

for the separator, where p is the porosity. Electrical resistivity in the axial (z) direction is dominated by the metal and is very low compared to the other materials. An analogous 'conduction in series' equation is used for the electrode assembly thermal conductivity in the radial direction, while the thermal conductivity (k) in the

Table 1
The effective material properties in a lithium ion battery.

Assembly	Direction	Wet thickness (μm)	Wet conductivity (W cm^{-1} K^{-1})	Wet specific heat (J g^{-1} kg^{-1})	Wet density (g cm^{-3})	Resistivity (Ω-cm)
Cathode	Radial Axial	109.224	0.0185 0.2049	1.1738	2.6175	25.7601
Anode	Radial Axial	192.632	0.0132 0.1778	1.0919	1.6714	25.4382
Half-anode	Radial Axial	100.316	0.0137 0.3194	0.9629	1.9618	24.4239
Package	Radial Axial	115	0.6197 0.0027	1.7194	1.7047	N/A

axial direction (conduction in parallel) is

$$k^{\text{axial}}_{\text{assembly}} = \frac{\sum t_i}{\sum t_i/k_i} \tag{11}$$

Assembly densities (ρ) are calculated as for the radial assembly resistivities, while the specific heats (C_p) are calculated by mass averages:

$$c_{p,\text{assembly}} = \frac{\sum t_i \rho_i c_{p,i}}{\sum t_i \rho_i} \tag{12}$$

The effective properties for prismatic lithium ion batteries provided by Manufacturer A are listed in Table 1. "Wet" properties represent the material properties after they are wetted with electrolyte.

3. Experiment

3.1. Entropy measurement

Entropy data of cathodes, anodes, and complete cells were obtained by monitoring the change in voltage as a function of temperature using the ETMS (Viaspace, ETMS-1000). Several cathode and anode powders were obtained from LICO Technology Corp. Cathodes and anodes were mixed with 85% active material, 10% PVDF, and 5% carbon black, and then cast on Al and Cu foil, respectively. Customer-coated cathode and anode films obtained from Manufacturer A were used as received for entropy measurement. To measure entropy changes in cathodes or anodes, they were assembled in a Type-2325 coin cell with a 0.75-mm-thick, Li-foil anode (Aldrich), a Celgard 2501 polypropylene separator and electrolyte (1 M $LiPF_6$ in EC/DMC [Merck]), using a coin cell crimper (National Research Council, Canada). Complete cells with $LiCoO_2$-based cathodes and graphite-based anodes from Manufacturer A also were assembled using a similar procedure to that described above by replacing Li metal with the graphite-based anode.

The cathode cells were cycled at $C/4$ rate between 3 and 4.1 V, with the cell potential held at the end values for 2 h to complete the charge or discharge. The voltage range for anode cells was 0.02–0.5 V. After three cycles, the cells were brought to a fully discharged state prior to the start of entropy determination. Charge stabilization was done at 35 °C for 2 h, followed by changing the cell temperature to the initial desired value. Typically, this initial temperature is set to be equal to charge stabilization temperature. After 15 min at this initial temperature, the cell voltage was measured, and then the cell temperature was changed to the next value (e.g., 25 °C). After temperature equalization at that temperature, the cell voltage was measured at the end of the period, and then the temperature was changed to the next level (e.g., 15 °C). The cell temperature was then brought to the initial value to determine deviation from the initial voltage reading. Entropy changes were calculated from the slope of the voltage–time curve using the equation $\Delta S = F[\delta \Delta E/\delta T)$, where F is the Faradaic constant. The experiments were repeated for $LiCoO_2$/graphite cells, using voltage limits of 4.2 and 2.5 V.

3.2. Temperature profile measurement during cycling of prismatic cells

Prismatic lithium ion batteries (using modified $LiCoO_2$/graphite) with nominal capacity of 4.5 Ah from Policell Technologies, Inc. were used for temperature measurements under different conditions. These batteries have eight cells stacked inside and have a dimension of 10 cm × 10 cm × 0.33 cm. These batteries were cycled by charging at $C/3$ rate to 4.2 V and discharging at $C/3$, C, $2C$, and $4C$ to 2.8 V using a BTS 500 battery cycler (Firing Circuits). The temperature on each face of a battery was monitored using type K thermocouples. A schematic location of the thermocouples is shown in Fig. 3. The battery was suspended in a Plexiglass frame to allow air exposure on all sides for convective cooling. Small aluminum clamps were attached to its electrode leads. Thermocouples were attached to both faces of the battery as shown in Fig. 3.

4. Experimental and simulation results

In our initial simulation, the entropies of $LiCoO_2$/C reported in Refs. [14,19] have been used to compare the effect of the entropy contribution to the battery temperature when (1) the average entropy of the complete battery was used and (2) the individual entropies of the anode and cathode were used in the simulations. Fig. 4 shows the temperature profile simulation for an eight-cell $LiCoO_2$/C prismatic battery. For clarity, only the temperatures that correspond to point 5 in Fig. 3 have been shown in Fig. 4. T_{center} and T_{surface} represent the temperatures at the center of eight-cell stack and on the surface of the package. The battery capacity was 4.8 Ah, the convective cooling coefficient was 0.001 W cm^{-2} °C^{-1}, and the ambient room air and battery initial temperature was 25 °C. Fig. 3 indicates that the effect of using of the battery-averaged entropy was to overestimate the predicted temperatures. When all other simulation parameters are the same, the temperature profile of the

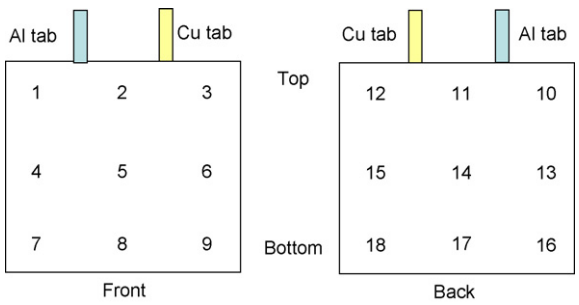

Fig. 3. Thermocouple locations in a prismatic lithium ion battery.

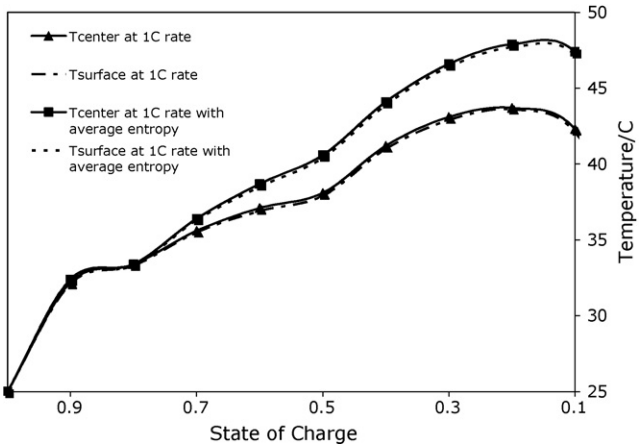

Fig. 4. Temperature profiles in a $LiCoO_2$/C battery with an eight bi-cell stack at various discharge states when discharged at the 1*C* rate.

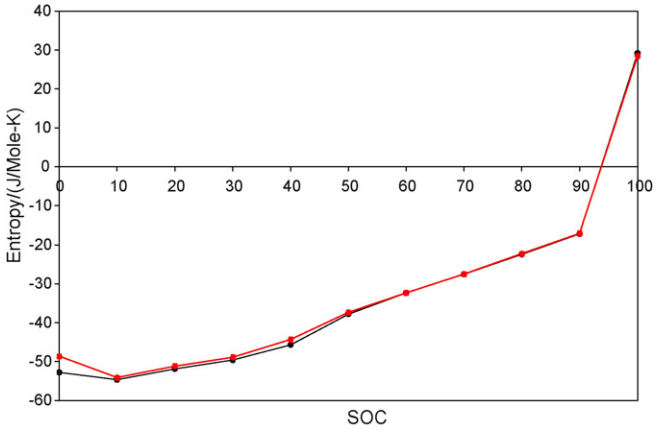

Fig. 6. Entropy changes for modified $LiCoO_2$ (vs. Li) prepared by Manufacturer A. Two curves in the figure represent the measured results on different days for the same cell.

battery is about 5 °C higher (during the later stages of the discharge) when the average battery entropy was used when compared to the profile obtained when separate entropies are used for the anode and the cathode. The reason for this difference is because different methods of averaging material properties result in different material properties. For best accuracy, it is recommended that material properties be averaged over volumes as small as possible. It also is interesting to note that no significant temperature difference was observed between the center (along the battery thickness direction and inside of the battery) of the stack and on the surface of the battery when this eight-cell battery was discharged at the 1*C* rate under natural ventilation conditions.

To obtain a better comparison between the simulation and experimental data, entropy changes for cathodes, anodes versus lithium metal and for complete cathode/anode combinations have been measured as a function of the SOC using the ETMS (Viaspace, ETMS-1000). Fig. 5 shows ΔS versus SOC for $LiCoO_2$ obtained from LICO Technology Corporation. Fig. 6 shows ΔS versus SOC for modified $LiCoO_2$ obtained from Manufacturer A. The two curves in the figure represent the measured results on different days for the same cell. In comparing the ΔS of $LiCoO_2$ shown in Fig. 1(a) with those in Figs. 4 and 5 (100% SOC at the right side of Figs. 4 and 5 corresponds to $x = 0.5$ at the left side of Fig. 1), it is interesting to note that all of the $LiCoO_2$-based cathodes show a valley in their entropy data at 10–20% SOC or $x \sim 0.9$. However, no peak at $x = 0.55$ or SOC = 90% was observed in Figs. 5 and 6. The difference between the entropy curves obtained from the $LiCoO_2$-based cathode may be attributed to the different manufacturing processes and impurity/doping used by different manufactures.

Fig. 7 shows ΔS versus SOC for $LiNi_xCo_yMn_zO_2$ obtained from LICO Technology Corporation. The agreement between two runs (shown as two separate curves in the figure) on different days for the same cell is reasonably good. It is of interest to notice that the entropy changes of the $LiNi_xCo_yMn_zO_2$ cathode shown in Fig. 7 are largely different as compared with the $LiCoO_2$ cathode shown in Figs. 5 and 6. First, the overall entropy change in $LiNi_xCo_yMn_zO_2$ is only 6 J mol^{-1} K^{-1}. The corresponding enthalpy change is 43.2 J mol^{-1} K^{-1}. However, Figs. 5 and 6 show that the overall entropy change in $LiCoO_2$ is more than 80 and 70 J mol^{-1} K^{-1}, respectively. The *larger* entropy change (mainly attributed to the change in configurational entropy [14]) represents a larger structure instability in $LiCoO_2$ than in $LiNi_xCo_yMn_zO_2$. We also noted that the largest entropy change in these two materials appears at two different charge states. For $LiNi_xCo_yMn_zO_2$, the largest entropy change appears when SOC = 0 (i.e., at the fully discharged state). For $LiCoO_2$, the largest entropy change appears at SOC ~ 20%.

Fig. 8 shows ΔS versus DOD (=1 − SOC) for a graphite-based anode obtained from Manufacturer A. The entropy data for graphite shown in Figs. 1(b) and 8 are very similar. In this case, the *x* axes on the left sides of both curves represent the fully lithiated state of

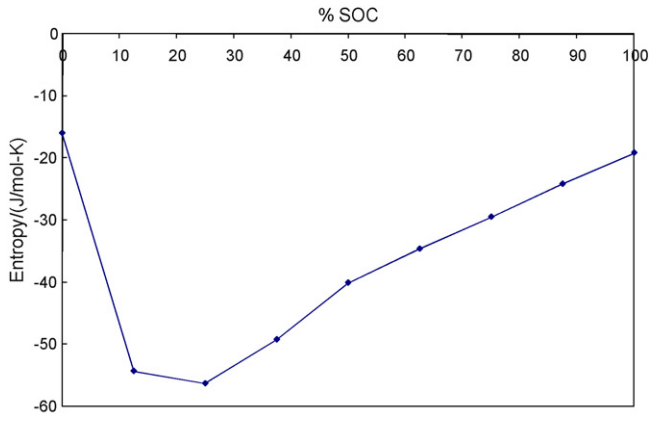

Fig. 5. Entropy changes for commercially available $LiCoO_2$ cathode (LICO Technology Corporation).

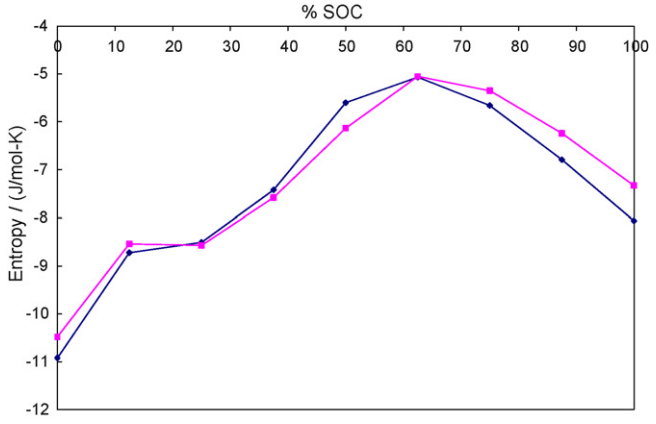

Fig. 7. Entropy changes for commercially available $LiNi_xCo_yMn_zO_2$ (LICO Technology Corporation). The agreement between two runs (shown as two separate curves in the figure) on different days for the same cell is reasonably good.

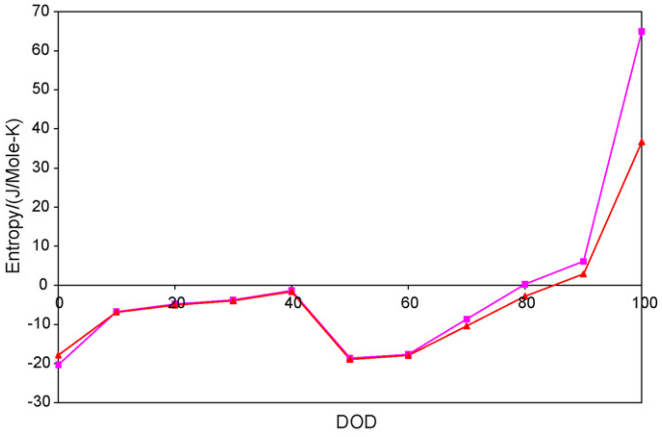

Fig. 8. Entropy changes for a graphite-based anode (vs. Li) prepared by Manufacturer A. The two curves in the figure represent the measured results on different days for the same cell.

graphite. The two curves in Fig. 7 represent the measured results on different days for the same cell. The entropy data for the complete coin cell using modified $LiCoO_2$ and graphite-based anode prepared by Manufacturer A is shown in Fig. 9.

Temperature profiles of prismatic lithium ion batteries during charge and discharge were measured for two conditions. Fig. 10 shows temperature profiles of the samples at the center of the sample (point 5 in Fig. 3) for an un-insulated 0.5 Ah Li-ion cell charged at the *C*/3 rate, and the discharged at *C*/3, *C*, and 2*C* rates. A small increase in temperature was observed at the end of charge. This increase probably was the result of the high impedance of the battery at extreme states of charge. The same pattern was evident during discharge at extreme states of charge. Interestingly, immediately after discharge when charging was commenced, the temperature decreased because charging for the Li-ion battery is endothermic. This is consistent with the thermal behavior of lithium ion batteries reported by Hong et al. [18]. Fig. 11 shows the temperature profiles at the center of the sample (point 5 in Fig. 3) for an insulated 4.5 Ah Li-ion cell charged at the *C*/3 rate, and the discharged at *C*/3, *C*, and 2*C* rates. In comparisons of Figs. 10 and 11, we found that the thermally insulated samples had a much slower temperature response, but the maximum temperature (45.5 °C) of the sample is higher than those of the air-cooled samples (36.4 °C).

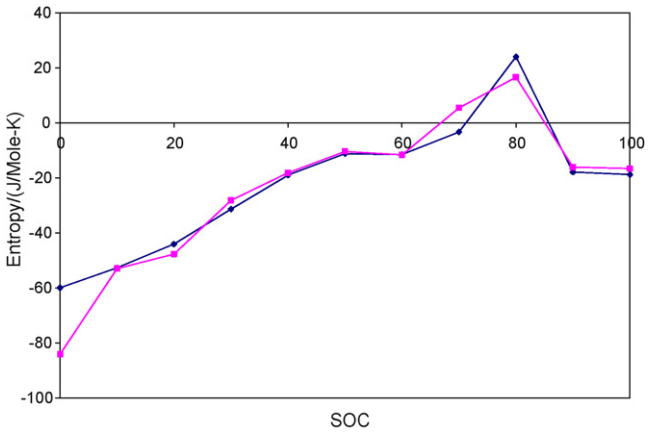

Fig. 9. Entropy changes for modified $LiCoO_2$ vs. a graphite-based anode prepared by Manufacturer A after cycling at the *C*/2 rate between 2.9 and 4.1 V. The two curves in the figure represent the measured results on different days.

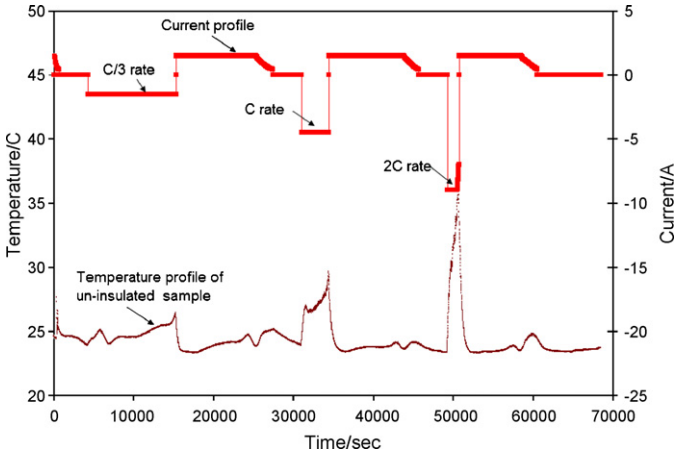

Fig. 10. Temperature profile at the center (point 5 in Fig. 2) of an un-insulated 4.5 Ah Li-ion cell charged at the *C*/3 rate, and then discharged at the *C*/3, *C*, and 2*C* rates.

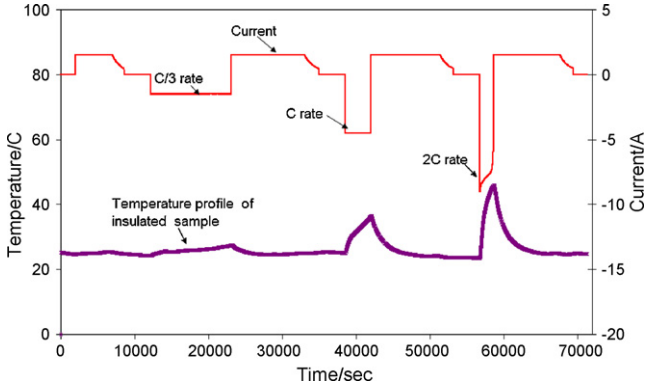

Fig. 11. Temperature profile of an insulated 4.5 Ah prismatic Li-ion cell charged at the *C*/3 rate, and then discharged at the *C*/3, *C*, and 2*C* rates.

The surface temperature variation of an un-insulated sample (4.5 Ah prismatic battery obtained from Policell Technologies, Inc.) was measured with multiple thermocouples (see Fig. 3 for the location of the thermocouples). Fig. 12 shows the temperature profile of the sample when discharged at the 3*C* rate. We found that the temperatures (at points 1, 2, 10, 11) around the positive terminal (i.e., the Al tab) are consistently higher (~5 °C) than those at the

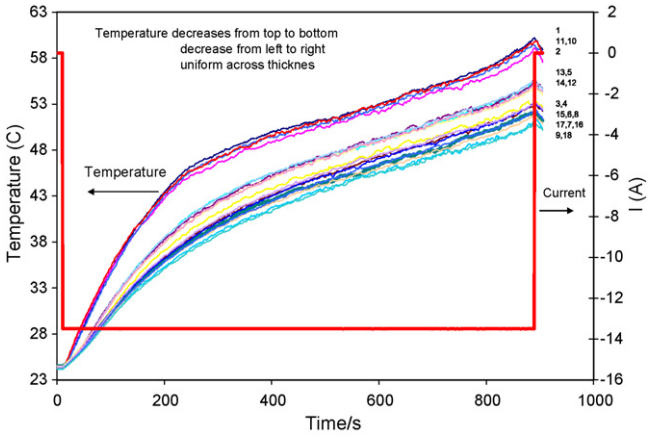

Fig. 12. The surface temperature profile of an un-insulated prismatic sample (4.5 Ah) (see Fig. 2 for the location of the thermocouples). The sample was discharged at the 3*C* rate.

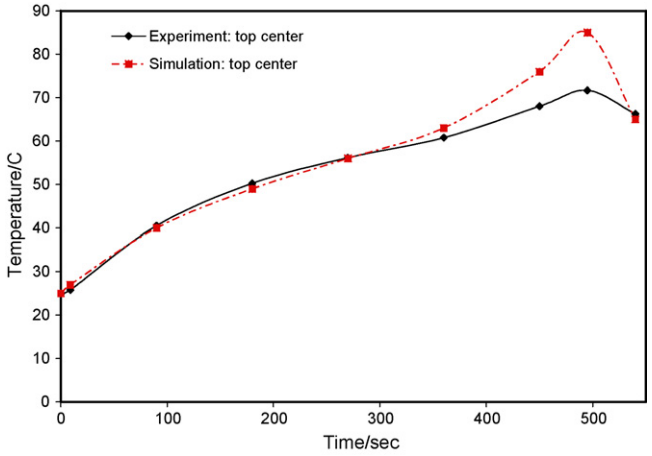

Fig. 13. Experimental and simulated temperature profiles for an eight-cell prismatic battery discharged at the 4*C* discharge rate.

negative terminal (i.e., the Cu tab). This finding is consistent with those observed by Pesaran et al. on cylindrical cells when the two terminals were on the same side [16]. We also found that the sample temperature decreased from the top (close to the tab area) to the bottom of the sample. Minimal temperature variations were observed between front and back of the sample.

5. Model performance compared to experimental results

Entropic heat generation terms were measured as a function of the DOD for each electrode material as described in Section 4. These results were used in the model described in Section 2. We found that heat loss along the tab area has a significant effect on the simulation results for prismatic batteries. The battery simulation consisted of solving for two primary unknowns: the heat transfer (1) from the leads/clamps and (2) from the convective cooling of the battery faces. Two sets of experiments at the 4*C* discharge rate were used for calibrating these heat-transfer conditions: one with the battery insulated, and one exposed to ambient (natural ventilation). The insulated case was used to eliminate convective cooling so that heat transfer from the tabs/clamps could be measured. Once heat transfer from the clamps was quantified, the air-exposed experimental data were used to calibrate the convective cooling on the large faces of the battery.

The heat transfer from the leads/clamps was measured by attaching three thermocouples to each tab/clamp. Thermocouples were attached to the clamps at 0.5, 1.0, and 1.5 in. (1.27, 2.54, and 3.81 cm) distances from the electrode tab/clamp interface. During the 4*C* discharge rate experiments, we found that the Al battery tab/clamp configuration exhibited a temperature gradient that would conduct heat away from the battery. However, the copper tab/clamp assembly exhibited a reversed temperature gradient that would conduct heat into the battery. The battery discharge was terminated at DOD = 0.55 ($t \sim 450$ s) because of the large IR drop at the 4*C* rate. At DOD = 0.55, the temperature gradients along the Cu tab were measured as $-10\,^{\circ}C/2.5$ cm and $+12\,^{\circ}C/2.5$ cm for the Al tab. The temperature gradients were reduced to essentially zero at DOD = 0.0. As a result, as discharge progressed, there was extra heat flowing through the top edge of the battery. Fig. 13 compares measured sample temperatures with simulated results. Nonlinearities in tab/clamp temperature gradients began at about 300 s. The convective coefficients were $C = 0.175\,W\,cm^{-2}\,^{\circ}C^{-1}$ and $n = 0.25$ (see Eq. (8)). The battery was cooled after discharge, and sample temperatures were continuously recorded. The lower measured temperatures after 300 s can be attributed to heat loss in the battery lead/clamp temperatures as discussed above. For more accurate comparisons, heat loss through both contact areas and thermocouples need to be considered.

6. Conclusions

The entropies in various cathode and anode materials, as well as complete Li-ion batteries, were investigated using the ETMS. We found that the detail shape of the entropy curves strongly depends on the manufacturer of the materials even for materials with the same nominal compositions. $LiCoO_2$ has a much larger entropy change than $LiNi_xCo_yMn_zO_2$. This means that $LiNi_xCo_yMn_zO_2$ is much more thermodynamically stable than $LiCoO_2$. The temperatures around the positive terminal a prismatic battery are consistently higher ($\sim 5\,^{\circ}C$) than those at the negative terminal. This is consistent with those observed by Pesaran et al. on cylindrical cells [16]. The effects of using battery-averaged entropies in the simulation tend to overestimate the predicted temperatures. When all other simulation parameters are the same, the temperature profile of a battery is about 5 °C higher (at the end of discharge) when the average-battery entropy is used when compared with profiles obtained from simulations in which individual entropies are used for the anode and the cathode. We also found it is interesting that no significant temperature gradient was observed at the center of the stack (i.e., inside of the battery) and on the outside surface of the battery in an eight-cell battery discharged at the 1*C* rate under natural ventilation conditions.

Acknowledgment

The research described in this paper was conducted under the Laboratory Directed Research and Development Program at Pacific Northwest National Laboratory, a multi-program national laboratory operated by Battelle for the U.S. Department of Energy.

References

[1] http://www1.eere.energy.gov/vehiclesandfuels/pdfs/program/phev_rd_plan_june_2007.pdf.
[2] http://online.wsj.com/article/SB118659859395791929.html?mod=hpp_us_whats_news.
[3] D. Bernardi, E. Pawlikowski, J. Newman, J. Electrochem. Soc. 132 (1985) 5.
[4] M. Doyle, T.F. Fuller, J. Newman, J. Electrochem. Soc. 140 (1993) 1526.
[5] J. Newman, W. Tiedemann, J. Electrochem. Soc. 142 (1995) 1054.
[6] C.R. Pals, J. Newman, J. Electrochem. Soc. 142 (1995), 3274 and 3282.
[7] M. Doyle, J. Newman, A.S. Dozdz, C.N. Schmutz, J.-M. Tarascon, J. Electrochem. Soc. 143 (1996) 1890.
[8] A. Funahashi, Y. Kida, K. Yanagida, T. Nohma, I. Yonezu, J. Power sources 104 (2002) 248.
[9] K.E. Thomas, J. Newman, J. Power Sources 119–121 (2003) 844–849.
[10] T. Araki, M. Nakayama, K. Fukuda, K. Onda, J. Electrochem. Soc. 152 (2005) A1128.
[11] K. Onda, T. Ohshima, M. Nakayama, K. Fukuda, T. Araki, J. Power Sources 158 (2006) 535.
[12] Y. Inui, Y. Kobayashi, Y. Watanabe, Y. Watase, Y. Kitamura, Energy Convers. Manage. 48 (2007) 2103–2109.
[13] S.-W. Kim, S.-I. Pyun, Electrochim. Acta 46 (2001) 897.
[14] Y. Reynier, J. Graetz, T. Swan-Wood, P. Rez, R. Yazami, B. Fultz, Phys. Rev. B 70 (2004) 174304.
[15] Y. Reynier, R. Yazami, B. Fultz, J. Electrochem. Soc. 151 (2004) A422.
[16] A. Pesaran, A. Vlahinos, D. Bharathan, NREL/AB-540-39502, December 2006.
[17] http://www.nrel.gov/vehiclesandfuels/energystorage/pdfs/39503.pdf.
[18] J.-S. Hong, H. Maleki, S. Al Hallaj, L. Redey, J.R. Selman, J. Electrochem. Soc. 145 (5) (1998) 1489.
[19] R. Yazami, Lithium Mobil Power, 1st ed., Knowledge Press, 2007, p. 167.
[20] D.K. Melgaard, R.F. Sincovec, ACM Trans. Math. Softw. 7 (1981) 106–125.
[21] J.R. Welty, C.E. Wicks, R.E. Wilson, Fundamental of Momentum, Heat and Mass Transfer, John Wiley & Sons, New York, 1969, p. 341.